

# An ultra-compact multiplexed holographic microscope using a multiple-pinhole aperture

Yujie Lu,<sup>1</sup> Yunhui Liu,<sup>1,2,\*</sup> Xiao Tian,<sup>1</sup> Yili Fu,<sup>2</sup> and Jie Zhao<sup>2</sup>

<sup>1</sup>Department of Automation and Mechanical Engineering, The Chinese University of Hong Kong, Shatin, N.T. 999077, Hong Kong, China

<sup>2</sup>State Key Lab on Robotics and Systems, Harbin Institute of Technology, The University Town of Shenzhen, Xili, Nanshan District, Shenzhen 518055, Guang Zhou, China

\*[yhliu@mae.cuhk.edu.hk](mailto:yhliu@mae.cuhk.edu.hk)

**Abstract:** In this paper, we present a low-cost and ultra-compact holographic microscope with multiple imaging areas. Instead of a dual-pinhole aperture as presented in our previous work, a multi-pinhole aperture is employed to filter the light source and to generate a reference wave as well as multiple object waves. The reference wave and the object waves interfere at the digital sensor and form multiplexed off-axis holograms without any lenses, splitters or combiners. The optimal number of object waves is determined which does not only fit our system but also brings some inspiration for traditional multiplexed off-axis holography. Our new system is tested to be able to retrieve quantitative phase images along with the amplitude images of multiple imaging areas at the same time with a lateral resolution of  $\sim 2.2\mu\text{m}$  and an accuracy of the optical path of tens of nanometers.

© 2015 Optical Society of America

**OCIS codes:** (090.1995) Digital holography; (120.5050) Phase measurement; (090.2880) Holographic interferometry.

---

## References and links

1. E. N. Leith and J. Upatnieks, "Reconstructed wavefronts and communication theory," *J. Opt. Soc. Am.* **52**, 1123–1128 (1962).
2. E. CuChe, F. Bevilacqua, and C. Depeursinge, "Digital holography for quantitative phase-contrast imaging," *Opt. Lett.* **24**, 291–293 (1999).
3. E. CuChe, P. Marquet, and C. Depeursinge, "Simultaneous amplitude-contrast and quantitative phase-contrast microscopy by numerical reconstruction of fresnel off-axis holograms," *Appl. Opt.* **38**, 6994–7001 (1999).
4. D. Gabor, "A new microscopic principle," *Nature (London)* **161**, 777–778 (1948).
5. L. Onural and P. D. Scott, "Digital decoding of in-line holograms," *Opt. Eng.* **26**, 261124 (1987).
6. W. Xu, M. Jericho, I. Meinertzhagen, and H. Kreuzer, "Digital in-line holography for biological applications," *Proc. Natl. Acad. Sci. U.S.A.* **98**(20), 11301–11305 (2001).
7. J. Garcia-Sucerquia, W. Xu, S. K. Jericho, P. Klages, M. H. Jericho, and H. J. Kreuzer, "Digital in-line holographic microscopy," *Appl. Opt.* **45**, 836–850 (2006).
8. E. CuChe, P. Marquet, and C. Depeursinge, "Spatial filtering for zero-order and twin-image elimination in digital off-axis holography," *Appl. Opt.* **39**, 4070–4075 (2000).
9. F. H. Mok, "Angle-multiplexed storage of 5000 holograms in lithium niobate," *Opt. Lett.* **18**, 915–917 (1993).
10. K. Curtis, A. Pu, and D. Psaltis, "Method for holographic storage using peristrophic multiplexing," *Opt. Lett.* **19**, 993–994 (1994).
11. M. Paturzo, P. Memmolo, A. Tulino, A. Finizio, L. Miccio, and P. Ferraro, "Multiplexing and demultiplexing of digital holograms recorded in microscopic configuration," *Proc. SPIE* 7390, 73901F (2009).

12. P. Picart, E. Moisson, and D. Mounier, "Twin-sensitivity measurement by spatial multiplexing of digitally recorded holograms," *Appl. Opt.* **42**, 1947–1957 (2003).
13. T. Saucedo A, F. M. Santoyo, M. De la Torre Ibarra, G. Pedrini, and W. Osten, "Simultaneous two-dimensional endoscopic pulsed digital holography for evaluation of dynamic displacements," *Appl. Opt.* **45**, 4534–4539 (2006).
14. C. Liu, Z. Liu, F. Bo, Y. Wang, and J. Zhu, "Super-resolution digital holographic imaging method," *Appl. Phys. Lett.* **81**, 3143–3145 (2002).
15. M. Paturzo, F. Merola, S. Grilli, S. De Nicola, A. Finizio, and P. Ferraro, "Super-resolution in digital holography by a two-dimensional dynamic phase grating," *Opt. Express* **16**, 17107–17118 (2008).
16. C. Yuan, H. Zhai, and H. Liu, "Angular multiplexing in pulsed digital holography for aperture synthesis," *Opt. Lett.* **33**, 2356–2358 (2008).
17. M. Paturzo and P. Ferraro, "Numerical aperture increasing in digital holography by a two-dimensional grating," in "LEOS Annual Meeting Conference Proceedings, 2009. LEOS'09. IEEE," (IEEE, 2009), pp. 127–128.
18. B. Sha, X. Liu, X.-L. Ge, and C.-S. Guo, "Fast reconstruction of off-axis digital holograms based on digital spatial multiplexing," *Opt. Express* **22**, 23066–23072 (2014).
19. P. Girshovitz and N. T. Shaked, "Real-time quantitative phase reconstruction in off-axis digital holography using multiplexing," *Opt. Lett.* **39**, 2262–2265 (2014).
20. J. Kühn, T. Colomb, F. Montfort, F. Charrière, Y. Emery, E. Cuche, P. Marquet, and C. Depeursinge, "Real-time dual-wavelength digital holographic microscopy with a single hologram acquisition," *Opt. Express* **15**, 7231–7242 (2007).
21. Z. Ma, Y. Yang, H. Zhai, and P. Chavel, "Spatial angular multiplexing for enlarging the detected area in off-axis digital holography," *Opt. Lett.* **38**, 49–51 (2013).
22. S. Boucherit, L. Bouamama, R. Zegadi *et al.*, "Formulation of off-axis single reference beam and two angle views for digital holography," *J. Opt.* **12**, 035302 (2010).
23. M. Paturzo, F. Merola, and P. Ferraro, "Multi-imaging capabilities of a 2d diffraction grating in combination with digital holography," *Opt. Lett.* **35**, 1010–1012 (2010).
24. P. Girshovitz and N. T. Shaked, "Doubling the field of view in off-axis low-coherence interferometric imaging," *Light Sci. Appl.* **3**, e151 (2014).
25. I. Frenklach, P. Girshovitz, and N. T. Shaked, "Off-axis interferometric phase microscopy with tripled imaging area," *Opt. Lett.* **39**, 1525–1528 (2014).
26. A. Greenbaum, N. Akbari, A. Feizi, W. Luo, and A. Ozcan, "Field-portable pixel super-resolution colour microscope," *PLoS ONE* **8**, e76475 (2013).
27. A. Greenbaum, Y. Zhang, A. Feizi, P.-L. Chung, W. Luo, S. R. Kandukuri, and A. Ozcan, "Wide-field computational imaging of pathology slides using lens-free on-chip microscopy," *Sci. Translat. Med.* **6**, 267–275 (2014).
28. Y. Zhang, A. Greenbaum, W. Luo, and A. Ozcan, "Wide-field pathology imaging using on-chip microscopy," *Virchows Archiv* **467**, 3–7 (2015).
29. Y. Lu, Y. Liu, and T. K. Lau, "Simple, portable, and low-cost microscope based on off-axis digital holography using two spherical waves," *Opt. Lett.* **39**, 4549–4552 (2014).
30. J. W. Goodman and S. C. Gustafson, "Introduction to fourier optics," *Opt. Eng.* **35**, 1513–1513 (1996).
31. M. Lee, O. Yaglidere, and A. Ozcan, "Field-portable reflection and transmission microscopy based on lensless holography," *Biomed. Opt. Express* **2**, 2721–2730 (2011).
32. N. Pavillon, C. S. Seelamantula, M. Unser, and C. Depeursinge, "Artifact-free reconstruction from off-axis digital holograms through nonlinear filtering," *Proc. SPIE* **7723**, 77231U (2010).
33. N. Verrier and M. Atlan, "Off-axis digital hologram reconstruction: some practical considerations," *Appl. Opt.* **50**, H136–H146 (2011).
34. J. Kennedy, "Particle swarm optimization," in "Encyclopedia of Machine Learning," (Springer, 2010), pp. 760–766.
35. G. Popescu, T. Ikeda, C. A. Best, K. Badizadegan, R. R. Dasari, and M. S. Feld, "Erythrocyte structure and dynamics quantified by hilbert phase microscopy," *J. Biomed. Opt.* **10**, 060503 (2005).
36. J. Kühn, F. Charrière, T. Colomb, E. Cuche, F. Montfort, Y. Emery, P. Marquet, and C. Depeursinge, "Axial sub-nanometer accuracy in digital holographic microscopy," *Meas. Sci. Technol.* **19**, 074007 (2008).
37. C. Mann, L. Yu, C.-M. Lo, and M. Kim, "High-resolution quantitative phase-contrast microscopy by digital holography," *Opt. Express* **13**, 8693–8698 (2005).
38. B. Rappaz, P. Marquet, E. Cuche, Y. Emery, C. Depeursinge, and P. Magistretti, "Measurement of the integral refractive index and dynamic cell morphometry of living cells with digital holographic microscopy," *Opt. Express* **13**, 9361–9373 (2005).

---

## 1. Introduction

In digital holography, off-axis configuration [1–3] can retrieve images with higher signal-to-noise ratio compared with Gabor inline set-up [4–7] as the so-called object term, zero order term

and twin image term are spatially separated. However, off-axis holography requires recording media with higher resolution so as to capture high frequency fringes in off-axis holograms. The resolution of the reconstructed object wave with off-axis geometry is much smaller than the resolution of the digital camera, as most part of the spectrum of the captured hologram is filtered out using the spatial filtering method [8]. What's more, among those abandoned spectrum, less than half is occupied by the noise terms (i.e. twin image term and zero order term) which implies the great potential of the off-axis holography to record more information with a single hologram.

Multiplexing is one of the alternative solutions to the aforementioned problem which has been extensively studied in holographic data storage [9–11], multi-dimensional measurement [12, 13], super-resolution imaging system [14–17], fast reconstruction of off-axis digital hologram [18, 19] and other areas [20, 21]. In 2010, Larbi's team [22] developed an off-axis imaging system which only uses a single reference wave and two object waves to form a multiplexed hologram. Their system simplified previous multiplexed off-axis systems where paired object waves and reference waves are applied. However, plenty of the spectrum in their system is still remained unused. In the same year, Merola's team [23] demonstrated a conciser approach to reconstruct multiple images from a single hologram by using a 2D diffraction grating. This system, yet, suffers from poor image quality and large redundant imaging area. In 2014, Shaked's team [24] presented a multiplexing approach named interferometry with doubled imaging area (IDIA) where a series of retro-reflectors and beamsplitters were added to manipulate one reference wave and two object waves. Later they improved their system by multiplexing another object wave [25]. Even though in the improved system they managed to make use of polarized light to avoid unwanted correlations of the object waves, the spectra of object terms of this system still partially overlapped with the spectra of zero order term and correlation terms. Thus high frequency noises may be introduced into the reconstructed images.

In recent years, a very promising lens-free on-chip microscope were proposed by Ozcan's team [26–28]. It utilizes a LED array or programmed stage to capture a 3D stack of lens-free images with inline set-up which could also retrieve both amplitude and phase image of the sample. The field of view (FOV) and image quality of this microscope are unattainable for other lens-free systems. However, as multiple low resolution holograms were employed (typically several hundred holograms), the dynamic performance of this kind of microscope is not as good as microscopes where only one hologram is used.

In our previous work [29], we presented a lens-free compact holographic microscope which features the advantages of both off-axis holography and Gabor inline holography. As the spatial filtering method is employed, our system shares the same disadvantage of off-axis holography where most of the spectrum of the recorded hologram is wasted. In order to address this problem, in this paper we propose an ultra-compact off-axis holographic microscope system that adopts a multiplexing method. Unlike other multiplexing imaging systems, we don't add any new optical components to our previous system which makes our system the most compact one. Besides, we quantitatively analyzed the maximum amount of information that can be obtained using our system. This not only suits for our system but also brings some inspiration on other multiplexed off-axis holographic systems.

## 2. System setup and basic principles

Fig.1 shows an illustration of our new system. A dual-pinhole aperture in our previous system is replaced by a multi-pinhole aperture (Provided by TianGong Laser Products Co.,Ltd, pinhole diameter:  $3\mu\text{m}$ ) to filter the light from a laser diode (LD-T650H00,  $\lambda = 650\text{nm}$ , measured power  $\approx 120\text{mW}$ ). One of those pinholes is designed as the reference pinhole while others are considered as the object pinholes. The projections of the image sensor on the sample plane

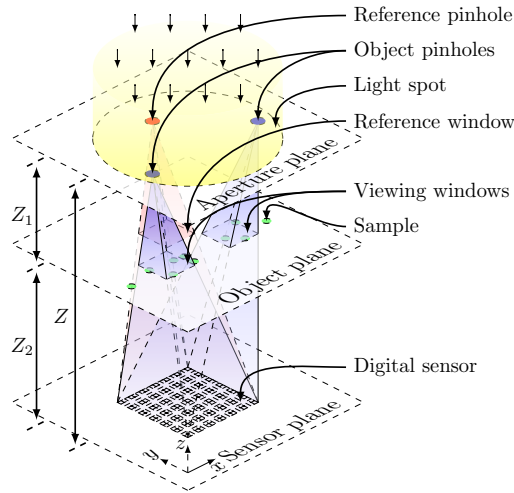


Fig. 1. System diagram (for simplicity, a triple-pinhole aperture is shown to illustrate the idea of the system. The number of pinholes includes but is not limited to three.)

with respect to the object pinholes are referred to as the viewing windows in the later part of the paper while the projection with respect to the reference pinhole is referred to as the reference window. The reference window should not be contaminated by the sample or overlap the viewing windows in order to generate the reference wave. The reference wave emitted from the reference pinhole and the object waves emitted from the object pinholes interfere at the image sensor (XIMEA, MQ042MG-CM, resolution:  $2048 \times 2048$ , pixels size:  $5.5 \mu\text{m}$ ) and form a multiplexed hologram. This grayscale hologram can be expressed as

$$I = |r(x,y) + \sum_{i=1}^{i=N} b_i(x,y)|^2, \quad (1)$$

where  $N$  is the number of object pinholes,  $r(x,y)$  is the reference wave, and  $b_i(x,y) (i \in \{1, \dots, N\})$  are the object waves. By expanding this equation, we can rewrite Eq. (1) as Eq. (2).

$$\begin{aligned} I &= (|r(x,y)|^2 + \sum_{i=1}^{i=N} |b_i(x,y)|^2) \\ &\quad + \sum_{i,j=1, i \neq j}^{i,j=N} b_i(x,y)b_j^*(x,y) + \sum_{i=1}^{i=N} [r^*(x,y)b_i(x,y) + r(x,y)b_i^*(x,y)] \\ &= z(x,y) + \sum_{i,j=1, i \neq j}^{i,j=N} c_{ij}(x,y) + \sum_{i=1}^{i=N} [o_i(x,y) + t_i(x,y)], \end{aligned} \quad (2)$$

where  $z(x,y) = |r(x,y)|^2 + \sum_{i=1}^{i=N} |b_i(x,y)|^2$  represents the zero order term,  $o_i(x,y) (i \in \{1, \dots, N\})$  represent the object terms,  $t_i(x,y) (i \in \{1, \dots, N\})$  denote twin image terms and  $c_{ij}(x,y) (i, j \in \{1, \dots, N\}; i \neq j)$  denote the correlation terms between the two object waves. As the different correlation terms may have the same frequency center, for simplicity, the correlation terms may be referred to as  $c_i(x,y) (i \in \{1, \dots, K\})$  in the later part of this paper.  $K$  is the number of correlation frequency centers which depends on the positions of the pinholes. Based on our previous analysis [29] and Eq. (2), the object waves of different viewing windows are modulated to different frequency centers. And the position of the frequency center of the  $i^{\text{th}}$  object term could be figured out using the following vector equation.

$$\vec{f}_i = \frac{\vec{d}_i}{Z\lambda}. \quad (3)$$

Here  $\vec{f}_i$  is the vector pointing from the origin to the frequency center of  $i^{\text{th}}$  object term and  $\vec{d}_i$  is the vector pointing from the reference pinhole to the  $i^{\text{th}}$  object pinhole. Therefore, the relative positions of the origin and frequency centers of the object terms are similar to the relative of the reference pinhole and the object pinholes. The radius of the spectrum of each object term can be represented as

$$f_{max} = \frac{1}{2M\delta}, \quad (4)$$

where  $M$  denotes the magnification factor of the system and  $\delta$  denotes the theoretical resolution of the optical system. It follows, if the resolution of the optical system is determined, we can still adjust the diameter of the object terms by changing the magnification factor of the system. With the separated positions and the controllable spectral radius, the object terms can be easily extracted by applying several special filters. Then, the images of different viewing windows can be rebuilt from the captured hologram using angular spectrum method [30].

### 3. System analysis and design

#### 3.1. Lateral resolution

As this system is based on our previous system which is a combination of Gabor inline holography and off-axis holography, most theories of both Gabor inline holography and off-axis holography are applicable to our new system. Hence the lateral resolution of the system is mainly limited by the size of pinhole, the numerical aperture (NA) and the magnification factor of the system.

The NA is the most important factor that limits the resolution of the optical part of the system which can be expressed as

$$NA = \frac{\frac{W}{2}}{\sqrt{(\frac{W}{2})^2 + Z_2^2}}, \quad (5)$$

where  $W$  represents the sidelength of the digital sensor and  $Z_2$  is the axial distance between the sample and the digital sensor. In our system, we utilize the imaging sensor with the sidelength of  $11.264\text{mm}$  and  $Z_2$  is designed as  $36\text{mm}$  (based on the design of the magnification factor, given by Eqn. (9), and the relationship among  $Z$ ,  $Z_1$  and  $Z_2$ ). As a result, our system possesses a NA of  $\sim 0.14$ .

The size of the pinhole is the other limiting factor of the resolution of the optical system. According to the previous literatures [7, 31], the size of pinhole affects the system resolution mainly in two aspects. First, the size of pinhole determines the size of the illuminating area. As we know, the imaging ability of Gabor inline holography comes from the interference fringes of inline reference wave and the object wave. When the illuminating area is smaller than the imaging sensor, the diffracted object wave cannot interfere with the reference wave at the unilluminated area of the pinhole which narrowed down the effective area of the digital sensor. As a consequence, the resolution of the system will be restricted. Second, for partially coherent Gabor inline systems, the spatial coherent diameter relies on the size of the pinhole. This does not apply to our system as the laser LED is used in our system. Hence if the digital sensor is fully illuminated, the resolution of the optical system will depend only on the NA, such that

$$\delta = \frac{\lambda}{2NA}. \quad (6)$$

For systems with  $3\mu\text{m}$  pinholes,  $Z$  is designed as  $39.5\text{mm}$  to ensure that.

Apart from previously discussed factors that could affect the resolving power of the optical system, the sampling and the reconstruction process may also lower the resolution of the entire system. Specifically, the magnification of the system should be large enough so that the spectra

of the object terms are confined to corresponding spatial filtering masks, or high frequencies signals will be filtered out during the spatial filtering process. This gives

$$M \geq \frac{1}{2f_d\delta}. \quad (7)$$

Here,  $f_d$  is the designed radius of the spatial filtering mask.

In the end, it is worth mentioning that, the resolution of the system is irrelevant to the number of object pinholes which disagrees with our first impression. Even though the increase of the number of pinholes will lead to the decreasing trend of  $f_d$ , if  $M$  is subject to the Ineq. (7), the shortened  $f_d$  will only result in a narrowed size of each viewing window but not the deduction of the resolution.

### 3.2. Design of the spectrum and the aperture

Till now, we have depicted a compact multiplex off-axis holographic system which is aimed at minimizing the waste of the spectrum of the hologram and making full use of it. Then, how many pinholes and what kind of pattern should be applied to achieve the best performance? Is it the more pinholes the better? To solve this problem, we need to quantify the amount of information that can be extracted so that we can evaluate the performance and make tradeoffs between the performance and the simplicity and feasibility of the system.

In off-axis holography, only the filtered object terms or twin image terms can be used to reconstruct the images of viewing areas. Thus if we define

$$\begin{aligned} \gamma &= \frac{\text{Area of used spectrum}}{\text{Area of the captured spectrum}} * 100\% \\ &= \frac{\sum \text{Area of the spectrum of the } i^{\text{th}} \text{ object term}}{\text{Area of the captured spectrum}} * 100\%, \end{aligned} \quad (8)$$

$\gamma$  represents the efficiency of the spectrum which to some extent reflects the total amount of information that could be reconstructed from a single hologram. To be more specific, if  $\gamma$  reaches 100%, it means that the zero order term and twin image term are perfectly eliminated, and the reconstructed images have the same resolution with the image sensor. On the contrary, if  $\gamma$  equals 0, it means that the spectrum is arranged so poorly that no uncontaminated object term could be obtained.

Before we proceed to the discussion of the maximization the efficiency of the spectrum, two issues still remain to be considered. First, overlapping should be avoided if the spectrum of the object wave is limited by a specific support, or high-frequency noise will be introduced into the reconstruction of the object wave. Second, the object terms should be located at the same half of the spectrum. As shown in Eqn. (3), the relative positions of the frequency centers of zero order term and the object terms in the spectrum map to that of the reference pinhole and object pinholes. Subsequently, if the object terms surround the zero order term, the object pinholes will also surround the reference pinhole which will result in a great difficulty of keeping the reference window clean while viewing the samples.

Let's consider the simplest situation where the number of object pinholes  $N = 2$ . Suppose the frequency of the sample is limited in a circular area with a radius which is set as the designed radius of the spatial filtering mask  $f_d$ ; the object terms and twin image terms are limited in the same spectral radius while the correlation terms and  $z(x,y)$  have a larger spectral radius of  $2f_d$ . According to geometrical considerations, same results of the maximum frequency of each object term could be derived as previous studies [32, 33] but two object waves are involved in this case. The distribution of the spectrum of this optimal configuration is illustrated in Fig. 2 (a). The rectangle illustrates the area of the spectrum which can be obtained by the digital

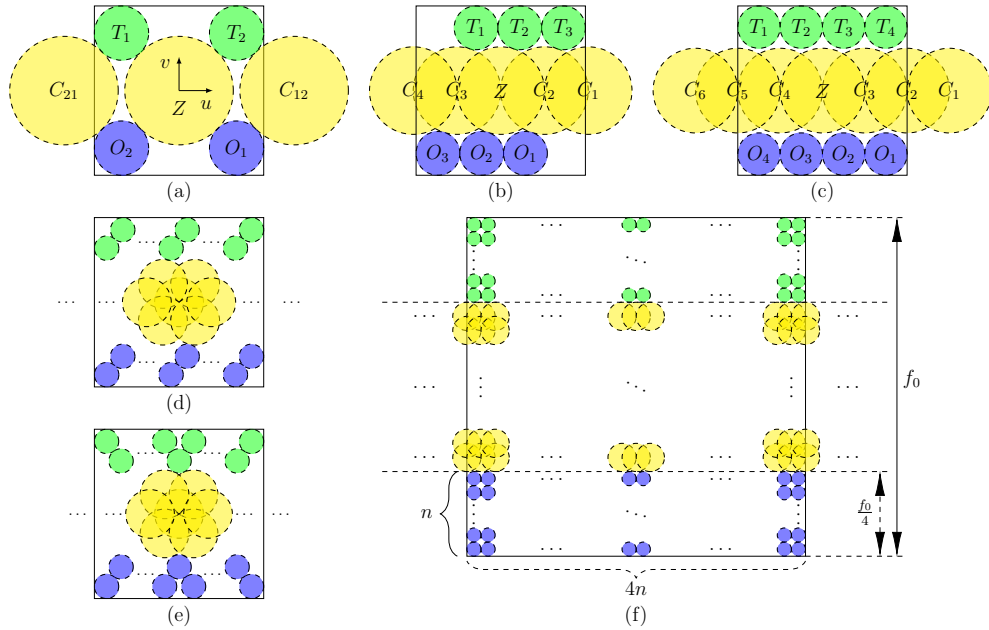


Fig. 2. Designed spectrum configurations when (a)  $N = 2$ , (b)  $N = 3$ , (c)  $N = 4$ , (d)  $N = 2k$  ( $k \in \{2, 3, 4, 5\}$ ), (e)  $N = 2k + 1$  ( $k \in \{2, 3, 4\}$ ) and (f)  $N = 4n^2$  ( $n \in \mathbb{Z}_+$ ).

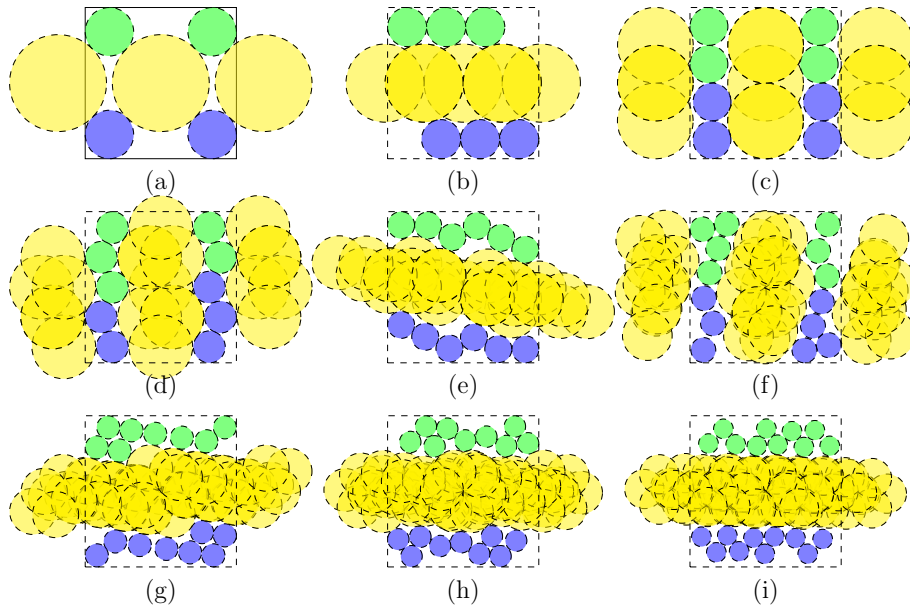


Fig. 3. Computer generated spectrum configurations for  $2 \leq N \leq 10$  using PSO method.

camera and the capitalized notations represent the spectrum or the Fourier transformation of the corresponding lower-case notations. The second object wave is modulated to the symmetric position of the first object wave with respect to the  $\nu$  axis of the spectrum. This configuration doubles the spectral efficiency to 16.12% without any adverse impact on the performance of each object wave.

When  $N \geq 3$ , the problem becomes more complicated. It is extremely difficult to find the global maximum of  $\gamma$ . Hence, we designed several simple patterns that may be close to the optimal solutions. In the first pattern, the object terms are positioned in one row at the bottom of the spectrum of the hologram. The spectra of the adjacent object terms are tangential to each other. Fig. 2 (b) - (c) show the spectrum of this kind of pattern when  $3 \leq N \leq 4$ . It is obvious that for  $N \geq 5$ , the spectral efficiency of this kind pattern will decrease as  $N$  increases. In order to gain higher  $\gamma$ , we designed another two patterns for  $N \geq 4$  as displayed in Fig. 2 (d) and (e). In these patterns, the object terms are arranged in two rows, one higher and one lower. The object terms in the higher row are tangential to the adjacent object term(s) in the lower row. When  $N = 2k(k \in \{2, \dots, 6\})$ , the object terms in the higher row are tangential to one correlation term, while when  $N = 2k + 1(k \in \{2, \dots, 6\})$ , the object terms in the higher row are tangential to two correlation terms at the same time. As  $N$  increases ( $N > 13$ ), the efficiency of two-row patterns will also decrease. That is when patterns with three or more rows should be adopted.

To verify the quality of previous designed pattern, we utilize particle swarm optimization(PSO) [34] to assist in searching for the optimal solutions. The resultant patterns are demonstrated in Fig. 3 and the efficiency of all aforementioned patterns are listed in Table 1. Comparing the patterns generated using PSO method with our designed pattern, it can be seen that for  $N = 2$  and 3, those patterns are exactly the same. For  $N = 4$  and 5, the generated patterns share the similar appearance with our designed ones. And the efficiency of those patterns are close to each other. For  $N > 5$ , the results of PSO method are even worse than our design. This may due to the reason that the optimization problem becomes so complicated as  $N$  increases that much more loops are needed to find better solutions. These results implies that our designed patterns of the spectrum are already close to the optimal solutions.

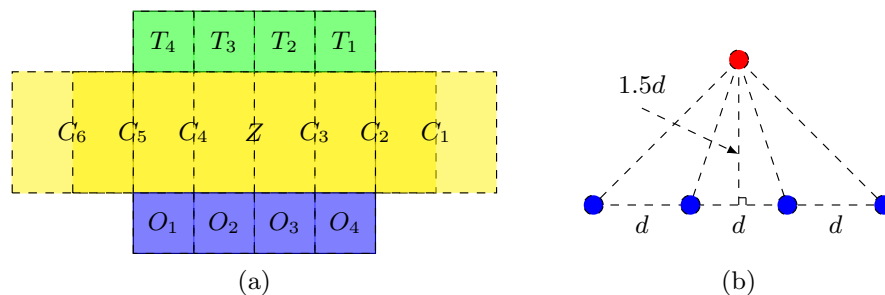


Fig. 4. (a) Adopted spectrum configuration and (b) corresponding layout of the aperture.

As  $N$  further increases, except for the object terms, more and more noise terms are added to the spectrum. This boosts the difficulties of the increase of the efficiency. Also, gaps between different object terms are unavoidable. Consequently, the spectrum efficiency of the optimal solution could barely increase or may even have a drop trend. For  $N = 4n^2(n \in \mathbb{Z}_+)$ , the efficiency of optimal solution should always larger than  $\pi/16$  ( $\approx 19.63\%$ ) which is the efficiency of the designed pattern as displayed in Fig. 2(f). Based on this and the previous results, we boldly conjecture that the efficiency of the optimal solution boosts only when  $N = 2$ , and for

$N \geq 3$ , the efficiency fluctuates around  $\pi/16$  and finally converges to it. As four is the smallest  $N$  where the efficiency reaches  $\pi/16$ , four should be the optimal number of the object waves while making compromises between the efficiency and the simplicity of the system. And four is the optimal number, to say the least, if we only consider  $N \leq 10$ . Inspired by this, four object pinholes are employed in our new system. As the efficiency of the designed patterns and the generated pattern when  $N = 4$  are almost the same, the simplest pattern shown in Fig. 2 (c) is adopted. In practice, we further replace the circular supports of the object term with square ones as illustrated in Fig. 4(a).

Table 1. Spectral efficiency of different patterns when  $N \leq 10$ .

| $N$      | 2      | 3      | 4      | 5      | 6      |
|----------|--------|--------|--------|--------|--------|
| One row  | 16.12% | 15.73% | 19.63% | –      | –      |
| Two rows | –      | –      | 19.66% | 17.43% | 15.36% |
| PSO*     | 16.12% | 15.73% | 19.67% | 17.43% | 14.96% |
| $N$      | 7      | 8      | 9      | 10     |        |
| Two rows | 15.98% | 15.21% | 16.50% | 16.33% |        |
| PSO*     | 14.81% | 14.64% | 14.17% | 13.20% |        |

\* Main parameters of PSO algorithm: Constrains: 1. The object terms can be captured by the digital sensor; 2. The object terms does not overlap with other terms; 3. The center of the object terms lies in lower half of the spectrum. Loops: 300. Maximum number of iterations (epochs) to train: 2000. Population size: 24.

Once the spectrum of the hologram is designed, the pattern of the aperture can be determined accordingly. Fig. 4(b) shows the layout of the pinholes. As  $\lambda = 650nm$  and  $Z = 39.5mm$ , the distance between the adjacent object pinholes ( $d$ ) equals to  $1.17mm$ .

### 3.3. Design of the magnification factor

In Irena's work [25], three separate imaging areas were obtained instead of a continuous one. This may be due to the reason that it is really difficult to adjust the positions or the sizes of each imaging area for such a complex optical system. For our system, however, it is very simple. All we have to do is adjust the size of the viewing window by changing the magnification factor until the adjacent viewing windows are connected to each other and constitute one bar-shaped viewing area. The magnification factor can be calculated using triangulations, such that

$$M = \frac{Z}{Z_1} = \frac{W + d}{d}. \quad (9)$$

This configuration is also subject to Ineq. (7). The proof is provided in Appendix A.

## 4. Experimental results and discussions

To verify the previous analysis of the lateral resolution, an amplitude resolution target (USAF 1951 T-22) was imaged using both our previous system and new system. In comparison with zebra-like fringes shown in Fig. 6(b), scale-like fringes can be observed as shown in Fig. 5 (b) which imply that multiple object terms are multiplexed to the hologram. This is confirmed by the spectrum of the hologram displayed in Fig. 5 (c) which is consistent with the designed pattern. Fig. 5 (d)-(g) denote the amplitude reconstructions of this multiplex hologram that demonstrate the system's ability to image four different viewing windows. Fig. 5 (h) illustrates a magnified area of Fig. 5(g). The width of the bars in the smallest resolvable elements equals

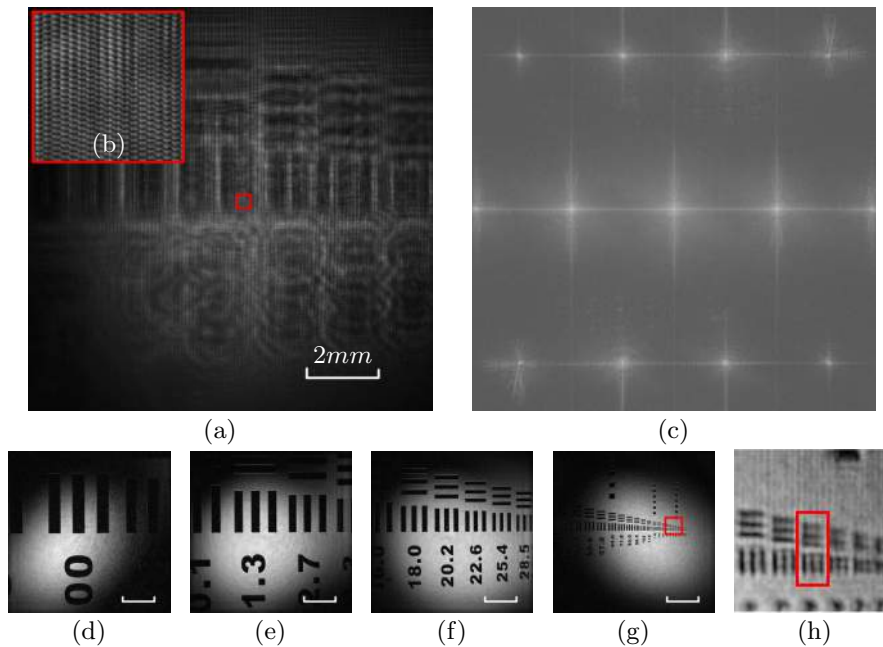


Fig. 5. Resolution test of our new system. (a) Multiplexed grayscale hologram of USAF 1951 T-22. (b) Enlarged highlighted part of (a). (c) Spectrum of the hologram. (d)-(g) Amplitude reconstructions of different viewing windows. The length of the white bar equals  $150\mu\text{m}$ . (h) Enlarged area of (g). The smallest resolvable elements are highlighted by a red rectangle. The width of those bars equals  $2.2\mu\text{m}$ .

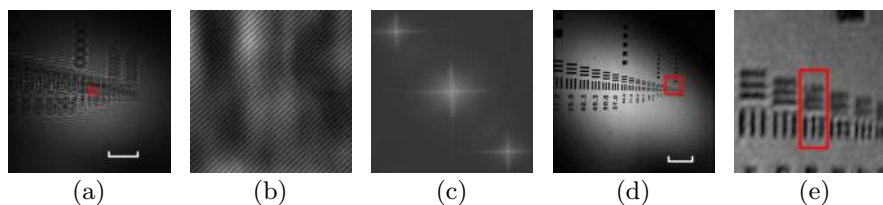


Fig. 6. Resolution test of our previous system. Source-sensor distance  $\approx 39.5\text{mm}$ , source-object distance  $\approx 3.5\text{mm}$ ,  $NA \approx 0.14$ , diameter of the pinholes =  $3\mu\text{m}$ , distance between the object pinhole and the reference pinhole =  $2.24\text{mm}$ . (a) captured hologram of USAF 1951 T-22. The length of the white bar equals  $2\text{mm}$  (b) Enlarged highlighted part of (a). (c) Spectrum of (a). (d) Amplitude reconstruction of (a). The length of the white bar equals  $150\mu\text{m}$ . (e) Enlarged area of (d). The highlighted elements are the same as the highlighted elements in Fig. 5(h).

$2.2\mu m$  which indicates that the resolution of the system reaches  $2.2\mu m$ . This is similar to the results demonstrated in Fig. 6(e) which is agree with our analysis.

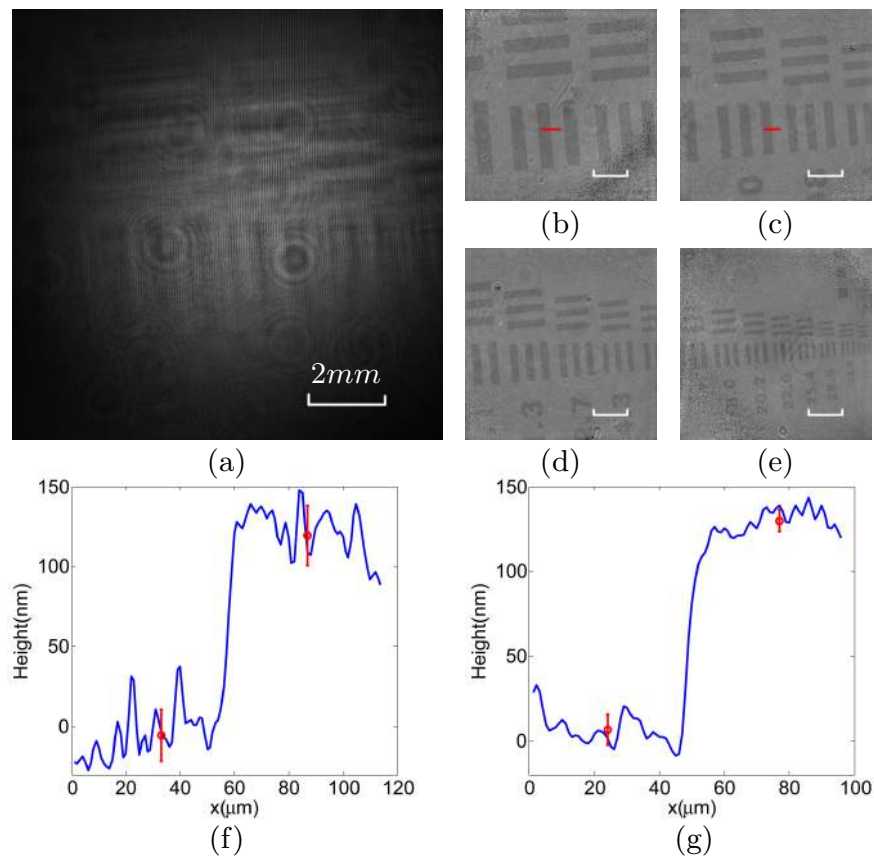


Fig. 7. Experimental results with the phase object using our new system. (a) The captured hologram. (b)-(e) The reconstructed phase image. (f) and (g) The surface profile of the highlighted line in (b) and (c). The red error bars show the means and standard deviations before and after the step.

Next, we try to evaluate the accuracy of the phase measurement of the system. To do this, we fabricated a transparent polydimethylsiloxane (PDMS) phase object using the amplitude resolution target as the mold. The height of the elements of the amplitude sample is measured as  $\sim 120nm$  using the Alpha-Step surface profiler. The height difference of the phase object should also be  $\sim 120nm$ . The hologram of this phase object was captured as displayed in Fig. 7(a). After reconstruction, the surface profile of this phase sample can be calculated from the phase reconstructions shown in Fig. 7(b)-(e). Fig. 7 (f) and (g) demonstrate the surface profile of the red bar in Fig. 7(b) and (c) respectively. The measured height differences are  $126.96nm$  and  $123.42nm$ . The standard deviations of these measurements before the step edge are  $15.51nm$  and  $9.14nm$ . After the step edge, the standard deviations are  $14.23nm$  and  $6.56nm$ . Here, we adopted 1.4 as the refractive index of the PDMS. It can be seen that the noise in the lateral viewing windows is higher than noise in the central ones as less direct light can reach the digital sensor through the lateral pinholes. As a result, the effective FOVs of the lateral windows may lower than the central ones. To evaluate the effective FOV, holograms without any objects

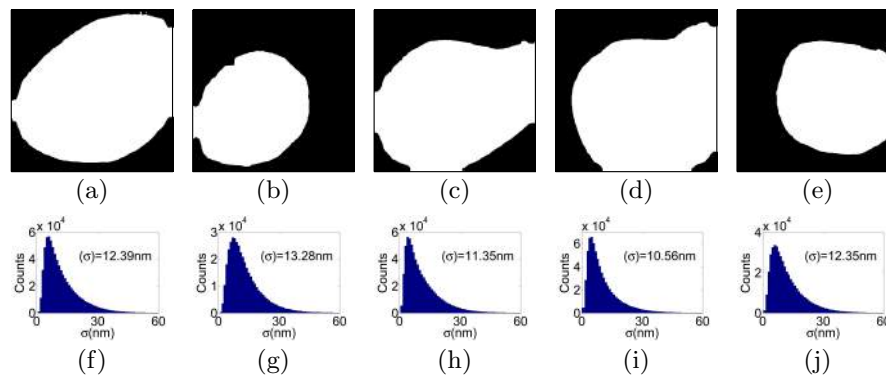


Fig. 8. (a)-(e) Effective FOVs. (f)-(j) Histograms of standard deviations corresponding to points within the effective FOVs. The average standard deviations ( $\sigma$ ) are provided. (a) and (f) are results of previous system. (b)-(e) and (g)-(j) are results of the proposed system.

were captured using both previous system and proposed system. Local standard deviation with a neighborhood size of  $101 \times 101$  were employed to estimate the noise and  $40\text{nm}$  were set as the threshold of the effective pixel. The resultant effective FOVs are shown in Fig. 8(a)-(e). Compared to our previous system, the effective FOV of the proposed system is about 3.1 times larger. And inside the effective FOVs, the histogram of the standard deviation and averaged standard deviations are provided which indicates our system possesses an accuracy of the optical path of tens of nanometers.

In the end, we further proved the feasibility of the system by conducting experiments with some biological samples. Fig. 9 and Fig. 10 show the experimental results with a slide of stained paramecia. The quantitative phase profile of a continuous bar-shape area can be retrieved using the proposed system. The cell structure of the paramecia could also be clearly obtained.

As we've mentioned in section 2, the fundamental assumption of our system is that the reference window should not overlap with the viewing windows or be contaminated by the samples. If an object lies in the reference window, the twin image of that object will appear in every reconstructed viewing window. Considering the fact that the reference window can be easily contaminated by one or more objects, samples that are carefully positioned or samples with a fixed sample support would be preferred. Besides, as the system can retrieve the amplitude and phase profile of a large bar-shape area from a single hologram, the dynamic performance of our system is better than systems that utilize multiple holograms. As a result, micro-channel-based fluidic applications are perfectly suited to our system.

## 5. Conclusion

We have illustrated a lens-free multiplexed off-axis holographic microscope with a multipinhole aperture. The optimal number of the object pinholes and the pattern of them were analyzed to maximize the information that could be retrieved from a single hologram. Based on our analysis, four should be the optimal number of the object pinholes which has been taken into practice. The spectral efficiency of our system reached 19.63% which is about 2.5 times larger than that of the traditional off-axis systems. The experimental results demonstrated that our system have the ability to obtain both the amplitude and phase information of four connected viewing areas. The total effective FOV of those viewing areas is 3.1 times larger compared with our previous system. The lateral resolution and the accuracy of the phase measurement were tested. Even through the accuracy of our system is inferior to that of the high-end sys-

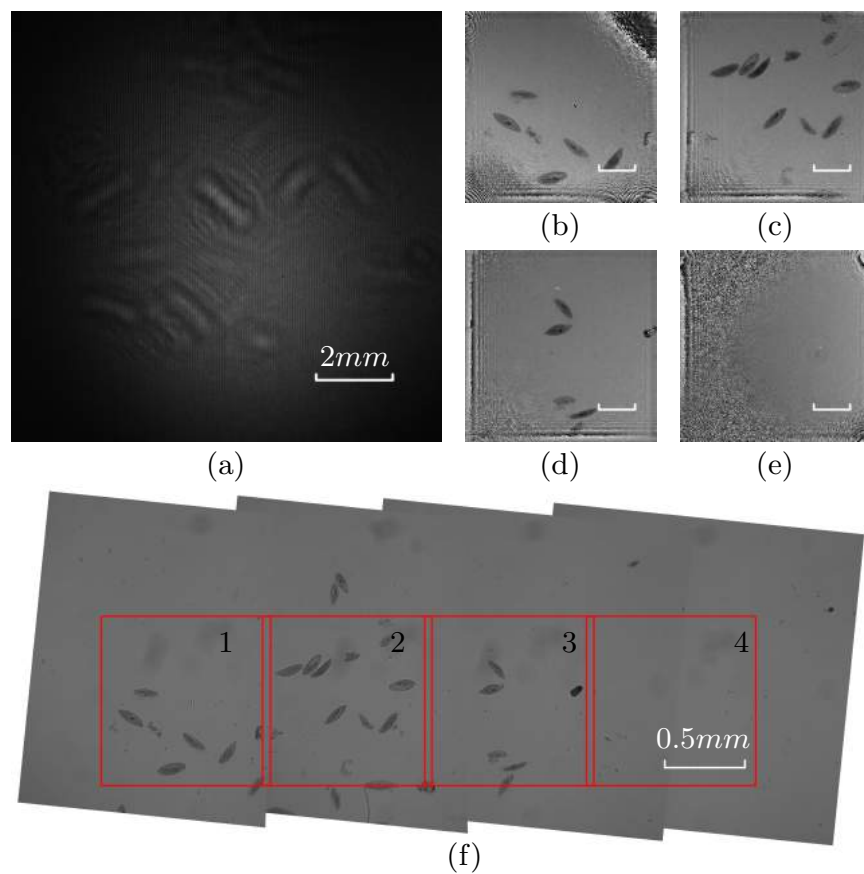


Fig. 9. Multiplexed hologram of paramecia and its reconstructed phase images. Source-sensor distance  $\approx 39.5\text{mm}$ , source-object distance  $\approx 3.5\text{mm}$ ,  $NA \approx 0.14$ . (a) Multiplexed grayscale hologram. (b) Enlarged highlighted part of (a). (c)-(f) Reconstructed phase images of different viewing windows. The length of the white bar in (c)-(f) equals  $200\mu\text{m}$ . (g) An image merged from four microscope photos with a  $10\times 0.25NA$  microscope objective is provided to illustrate the imaging area of the system. The red rectangles 1-4 specify the size and position of the reconstructed viewing windows of (c)-(f).

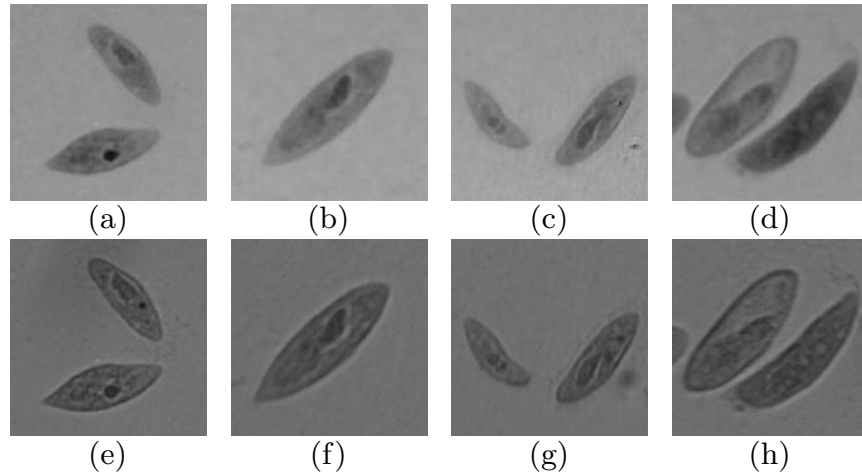


Fig. 10. (a)-(d) Enlarged phase images of paramecia from Fig. 9. (e)-(f) Microscope images captured with 10x 0.25NA microscope objective.

tems [35, 36], our accuracy within the effective FOVs are competitive with the accuracy of other systems [37, 38]. And consider the cost-effectiveness of our system, our system could be useful in many biological applications.

## 6. Acknowledgement

This work is supported in part by the Hong Kong Innovation and Technology Fund via project ITS/089/13, State Key Laboratory of Robotics and System (HIT) via Self-Planned project NO. SKLRS201401B and the Shenzhen Research and Development Fund via project JCYJ20140417172417120.

## Appendix A

Proof:  $M \geq \frac{1}{2f_d\delta}$  when  $M = \frac{W+d}{d}$ .

From Eq. (3), we can derive that the shifted frequency between two adjacent object terms can be illustrated as

$$f_{sh} = \frac{d}{Z\lambda}. \quad (10)$$

As the spectra of the two object terms are tangential to each other,

$$f_d = \frac{f_{sh}}{2} = \frac{d}{2Z\lambda}. \quad (11)$$

Substituting Eq. (9) and (11) into left side of the inequation, we will get

$$\begin{aligned} M &= \frac{W+d}{d} \\ &= \frac{W+d}{2\lambda Z f_d}. \end{aligned} \quad (12)$$

According to the relations between  $Z_1$ ,  $Z_2$  and  $Z$ , we have

$$Z = \frac{M}{M-1} Z_2 = \frac{W+d}{W} Z_2. \quad (13)$$

Then we can further rewrite the left side of the inequation, such that

$$M = \frac{W}{2\lambda Z_2 f_d}. \quad (14)$$

The resolution of the system can be estimated as

$$\delta = \frac{\lambda}{2NA} = \frac{\lambda \sqrt{(\frac{1}{2}W)^2 + Z_2^2}}{W} \approx \frac{\lambda Z_2}{W} \quad (15)$$

Then,

$$\text{Right side} \lesssim \frac{W}{2\lambda Z_2 f_d} = \text{Left side}. \quad (16)$$